Software Calibration of a Frequency-Diverse, Multistatic, Computational Imaging System

Yurduseven, O., Gollub, J., Trofatter , K. P., Marks, D., Rose, A., & Smith, D. (2016). Software Calibration of a Frequency-Diverse, Multistatic, Computational Imaging System. IEEE Access, 4, 2488-2497. https://doi.org/10.1109/ACCESS.2016.2570678

Published in:
IEEE Access

Document Version:
Publisher's PDF, also known as Version of record

IEEE Access
Multidisciplinary | Rapid Review | Open Access Journal

Received April 23, 2016, accepted May 17, 2016, date of publication May 19, 2016, date of current version June 13, 2016.

Digital Object Identifier 10.1109/ACCESS.2016.2570678

Software Calibration of a Frequency-Diverse, Multistatic, Computational Imaging System

OKAN YURDUSEVEN[1], (Member, IEEE), JONAH N. GOLLUB[1], (Member, IEEE), KENNETH P. TROFATTER[1], DANIEL L. MARKS[1], ALEC ROSE[2], AND DAVID R. SMITH[1], (Member, IEEE)

[1]Center for Metamaterials and Integrated Plasmonics, Department of Electrical and Computer Engineering, Duke University, Durham, NC 27708, USA
[2]Evolv Technologies, Inc., Waltham, MA 02451, USA

Corresponding author: O. Yurduseven (okanyurduseven@ieee.org)

This work was supported by the Science and Technology Directorate within the Department of Homeland Security under Contract HSHQDC-12-C-00049.

ABSTRACT We demonstrate a technique for calibrating a frequency-diverse, multistatic, computational imaging system. A frequency-diverse aperture enables an image to be reconstructed primarily from a set of scattered field measurements taken over a band of frequencies, avoiding mechanical scanning and active components. Since computational imaging systems crucially rely on the accuracy of a forward model that relates the measured and transmitted fields, deviations of the actual system from that model will rapidly degrade imaging performance. Here, we study the performance of a computational imaging system at microwave frequencies based on a set of frequency-diverse aperture antennas, or panels. We propose a calibration scheme that compares the measured versus simulated scattered field from a cylinder and calculates a compensating phase difference to be applied at each of the panels comprising the system. The calibration of the entire system needs be performed only once, avoiding a more laborious manual calibration step for each transmitting and receiving path. Imaging measurements performed using the system confirm the efficacy and importance of the calibration step.

INDEX TERMS Frequency-diversity, computational imaging, software, calibration, near-field.

I. INTRODUCTION

Computational imaging approaches offer many advantages that can address the challenges associated with conventional imaging schemes, such as synthetic aperture radar (SAR) and phased arrays—two of the most widely used imaging techniques in the literature. These two techniques cover a host of applications, including security-screening [1]–[3], remote sensing and terrestrial imaging [4], and biomedical applications [5], [6]. Although good image fidelity can be achieved with these methods, they nevertheless have well-known limitations. SAR systems, for example, are limited in terms of acquisition speed, while phased arrays and electronically scanned antennas are necessarily complex systems that exhibit large power consumption, tend to be expensive, and are often significant in terms of weight and size.

For an imaging system, it is desirable to reduce the imaging time and system cost, and simplify the hardware architecture while obtaining high fidelity images. The overall imaging time is determined by the combination of the rate of the data acquisition and the image reconstruction time. Data acquisition time can be significantly reduced through the use of an electronically reconfigurable aperture to steer a beam or form radiation patterns, rather than using mechanical scanning equipment and fixed pattern antennas. However, conventional approaches for dynamic apertures typically require active components, increasing the system complexity and cost, such as in phased arrays.

With the advent of high speed computing, modern imaging systems increasingly have the opportunity to take advantage of computational imaging concepts [7]–[9], which enable greater flexibility in terms of the physical hardware design. Computational imaging schemes necessitate precise knowledge of the antenna field patterns, combined with specific models of object scattering, to form a complete forward model of the system that can be used to reconstruct a scene from a set of measurements. The advantage of the computational imaging approach is that many alternative antenna designs and corresponding radiation patterns can be integrated into the system design, with numerical processing playing a greater role in the ultimate image reconstruction. The challenge of such schemes is that any deviation from the forward model will inevitably degrade the imaging performance—sometimes drastically. The situation is especially acute for coherent imaging schemes, which rely on the

interference of often complex field patterns, whose phase and amplitude must be known to exacting tolerances.

Recently, a computational imaging system based on the use of frequency-diverse aperture antennas has been demonstrated at microwave frequencies [10]–[18]. In a frequency-diverse imaging system, a scene is sampled using antennas producing frequency-dependent radiation patterns that exhibit complex spatial field patterns. As the frequency is swept, the fields radiated by the imaging antennas sample different sub-sections of the imaging domain, encoding the scene information onto a set of measurements at a set of discrete frequencies. Leveraging computational-imaging algorithms, the frequency-encoded information can be used to reconstruct the scene. This process does not involve mechanical scanning or active circuit components.

One method of achieving a frequency diverse antenna is to populate the upper conductor of a planar waveguide structure with resonant, complementary, metamaterial elements, which couple to the local field within the waveguide and radiate into the scene [10]–[14]. A waveguide mode excited within the parallel plate structure excites the metamaterial elements, each having a different resonant frequency selected from within an operating bandwidth. With the resonance frequencies of the elements chosen randomly, at any particular drive frequency the radiation pattern emerging from the planar antenna will be distinct, with the total number of distinct modes over the frequency band set by the quality factor (Q-factor) of the resonant metamaterial elements. Since the Q-factor of the antenna ultimately sets the number of distinct measurement modes (or spatially distinct radiation patterns), an alternative configuration is to use a closed cavity resonator with a smaller number of radiating irises. Enclosing the parallel plate waveguide with conducting walls and reducing the number of radiating elements increases the Q-factor considerably [15]–[17]. In the system presented here, we use a recently demonstrated printed cavity antenna design, consisting of an array of radiating irises distributed in a Mills Cross pattern [18] (see Fig. 1). The Mills Cross pattern, created by the overlap of the iris patterns on the transmit and the receive antennas, maximizes coverage of the scene in Fourier space, improving the orthogonality of the field distributions in the scene space [19].

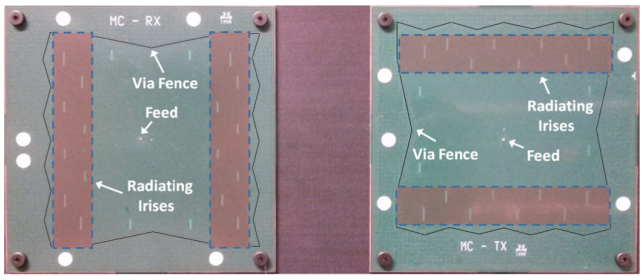

FIGURE 1. Mills Cross cavity antennas (a) receive (b) transmit.

Calibration is an important task necessary for all imaging systems, but is particularly critical for coherent imaging systems as well as computational imaging systems. For the multistatic, frequency-diverse imaging system considered here, which consists of an array of transmitting and receiving aperture antennas, system calibration is needed specifically to correctly determine the phase centers of the antennas [20]–[23]. Since a phase error translates to a spatial offset in the range direction, the accumulation of phase errors can result in each antenna reconstructing a given object on a different plane, causing reconstruction algorithms to produce distorted images or even fail completely.

For computational imaging systems, a detailed model is required to establish the relationship between the fields generated by the antennas and those at the objects being imaged – which we refer to as the *forward model*. Calculating the forward model requires knowledge of the fields radiated from the antennas. The field patterns can be obtained using analytical models, such as the dipole approximation in [14], or measurements, such as near-field scanning of the antennas in [16]. Any errors involved in the forward model, such as misalignment of the antennas or inaccurate information of the fields radiated by the antennas will degrade the image reconstruction. This challenge is magnified in a frequency-diverse system where the antennas produce complex radiation patterns that vary strongly as a function of frequency.

Since coherent, computational imaging methods also require absolute knowledge of the phase, the accuracy of the forward model consequently depends on characterization of the phase of all radio frequency (RF) paths in the system. Such paths include all cables, switches and connectors between the antennas and the RF signal source, which we refer to here as *RF connections*. As we discuss in the next section (specifically for multistatic, near-field imaging systems), any error in phase characterization of the RF connections will exhibit itself as effective noise in the reconstructed image. Therefore, calibrating these contributors is critical.

In this paper, we demonstrate a practical calibration method for a frequency-diverse, multistatic imaging system. The proposed method relies on the use of a calibration target (a metal cylinder) to calculate the additional phase difference introduced by the RF connections in the system. By comparing the simulated and measured signals reflected from the calibration object, we obtain the phases introduced by the RF connections for all transmitting and receiving paths and are thus able to compensate for these effects. The proposed calibration technique is a one-step procedure and circumvents the requirement of performing a manual calibration for each transmitting and receiving path within the system. This significantly simplifies the calibration procedure and shortens the amount of time required for system calibration.

II. CALIBRATION OF THE SYSTEM

Coherent imaging systems require accurate phase knowledge of the system to achieve imaging. This is especially important for multistatic imaging systems consisting of an array of transmitting and receiving antennas. Unaccounted for RF connections between the signal source and the antennas can

significantly destroy the image reconstruction. It is therefore necessary to calibrate the RF connections in the system in such a manner that all aperture antennas effectively possess a common phase. A straightforward way of achieving this calibration is to remove each cable from the system and perform a transmission (S_{21}) measurement to obtain the phase advance. The measured phase advance can then be removed from the signal received from the imaging object when the RF connections are attached to the system. We refer to this process as *manual calibration*.

While manual calibration is feasible for systems with a small number of antennas, as the number of the transmitting and receiving antennas increases, manual calibration of the RF connections becomes labor-intensive and time-consuming. For an imaging system consisting of T transmitting and R receiving antennas, the number of total RF paths to be calibrated is $T \times R$. For example, the frequency-diverse imaging system considered in this work consists of 16 transmitting and 48 receiving antennas, suggesting that, if done manually, 768 different RF paths need to be calibrated on an individual basis. One could calibrate each transmitting and receiving path separately and then combine their responses to determine the full set of calibration paths, resulting in $T+R = 64$ S_{21} measurements being taken. However, this still requires considerable effort and attention to measurement accuracy. As an alternative, a semi-automated calibration procedure can be applied to compensate for the additional phase advance introduced by each of the RF paths (including all RF connections – i.e. cables, connectors and switches). In this approach, we place a target in the scene with known scattering characteristics and measure the phase of the received signal from each transmitting and receiving antenna pair within the system. We then model the experimental configuration in a simulation platform, comparing the measured signal to the simulated signal to calculate the phase shift caused by the RF connections. This single-step procedure does not require further iterations for different RF paths.

As calibration target, we use a metal cylinder with a diameter of 7.5 cm and a length of 2.1 m. Using a cylinder target provides strong specular reflection, and hence return signal, at some place on the target for all transmitting/receiving combinations. Moreover, it has a well-defined analytic description (quadric surface), making the cylinder structure easy to fit and define in simulations [24]. For the implementation of a cylindrical target as a calibration object, one might consider creeping waves as a challenge. However, it should be noted that the primary information obtained from the measurements is the group delay of the signal reflected from the cylindrical target. The reflection from the specular target may be largely approximated using a geometric diffraction approximation as being from the specular point, or the point that is the image of transmit antenna after being reflected from the surface of the cylinder, the cylinder acting as a portion of a toroidal mirror. The creeping wave arrives later and is a much smaller contribution to the return signal. As the specular return is both much stronger and separated in time from the creeping wave, the creeping wave has little effect on the group delay estimate.

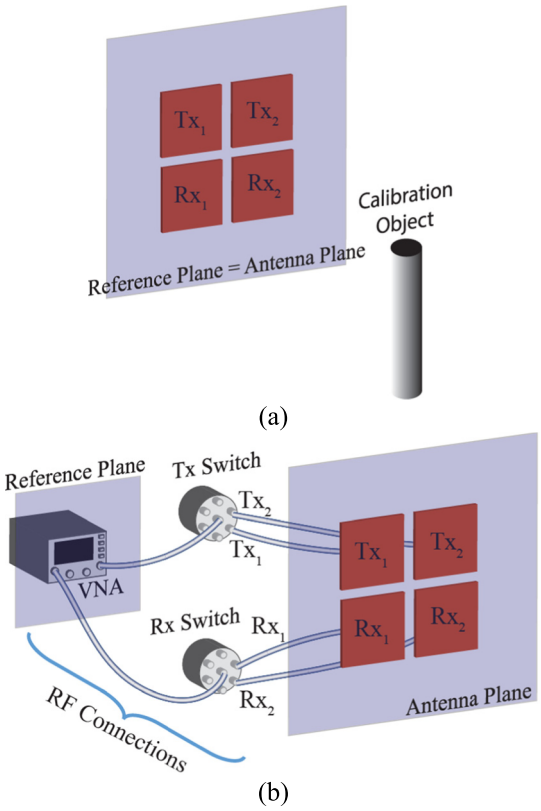

FIGURE 2. Imaging configurations (a) simulation (Virtualizer) layout (b) experimental layout.

The entire imaging environment, from the antenna plane to the scene, can be modelled using a Matlab-based simulation platform referred to here as the *Virtualizer* [14]. The phase reference plane for the simulated system is coincident with the plane of the antennas illuminating the calibration object. The details of the RF connections and other aspects of the physical system are not modelled directly, though an arbitrary phase advance can be added in the software to each simulated antenna. In Fig. 2, we depict the simulation and experimental imaging system layouts for an imaging system consisting of two transmitting and two receiving antennas. As shown in Fig. 2(a), for the simulations, the reference plane for imaging (i.e., the plane from which the signal is transmitted and at which the reflected signal is received) is identical to the antenna plane. For the experimental system layout in Fig. 2(b), the reference plane is defined at the ports of the RF signal source, a vector network analyzer (VNA, Agilent N5245A), and the RF connections lie in between the antenna and phase reference planes. The goal of an automated calibration procedure is to create a common reference plane that coincides with the antenna plane by removing all extraneous phase advances introduced by the cabling. This calibration is achieved by comparing the

experimentally measured signal collected from the calibration target to the simulated signal.

The frequency-diverse imaging system considered in this work operates in the K-band regime, 17.5-26.5 GHz, discretized into 101 frequency points. In the Virtualizer, a forward model is used for the imaging problem that includes the propagating fields from and to the antenna plane, using the first Born approximation to model scattering from objects within the scene.

The forward model is used to create a measurement matrix that correlates a set of signal measurements to the susceptibility of voxelized objects in the scene as follows:

$$\mathbf{g}_{Mx1} = \mathbf{H}_{MxN}\mathbf{f}_{Nx1} + n \tag{1}$$

In (1), $\mathbf{g}$ is the signal received from the calibration object, $\mathbf{H}$ is the measurement matrix, $\mathbf{f}$ is the susceptibility vector corresponding to those voxels comprising the calibration object and n represents a noise term. The number of measurement modes is given by M while the scene is discretized into N voxels. Elements of the measurement matrix, $\mathbf{H}$, are proportional to the fields radiated by the transmitting, $\mathbf{E}_{\mathrm{Tx}}$, and receiving, $\mathbf{E}_{\mathrm{Rx}}$, antennas evaluated at the position of a given voxel, such that $\mathbf{H}_{i,j} \propto \mathbf{E}_{i,j}^{Tx}\mathbf{E}_{i,j}^{Rx}$ (calculated at frequency f_{i} and at position $\mathbf{r}_{\mathrm{j}}$). In other words, the $\mathbf{H}$ matrix is proportional to the dot product of the transmitting and receiving vector fields, $\mathbf{E}_{\mathrm{Tx}}$ and $\mathbf{E}_{\mathrm{Rx}}$. While the radiated fields from the antennas can be simulated, to ensure exact agreement with the experiments we use a near-Field scanner (Near-Field Systems Inc., NSI 200 V-3 x 3) [16] to directly measure the fields over a plane close to a given antenna, using a relatively large field-of-view (FOV), with angular range of $\pm 60°$. We assume that the accuracy of the near-field scan measurements and the selected FOV are sufficient so as not to introduce any significant source of error. The measured fields can be propagated throughout the imaging domain using dyadic Green's functions [11].

The measured fields radiated by the antennas are used to calculate the $\mathbf{H}$ matrix. The Virtualizer can then be used to simulate the expected $\mathbf{g}$ from a virtualized cylinder, assuming the phase reference plane is coincident with the antenna plane, as depicted in Fig. 2(a). For the experimental system, the measured $\mathbf{g}$ includes the phase advances from the antennas in addition to the phase advances through the distribution paths between the reference and antenna planes, as depicted in Fig. 2(b). Therefore, it is necessary to calibrate the system such that the reference plane of the system is effectively brought to the antenna plane. It should be noted that we use the term distribution path to refer to the paths containing all RF connections between the VNA and the individual transmitting and receiving antenna pairs as shown in Fig. 2(b). The distribution path can be considered as part of the propagation path, which, in addition, includes the path between the antennas and the scene.

Consider the fields radiated by a single frequency-diverse antenna, Rx_1, in the experimental system shown in Fig. 2(b). For this example, we assume that an RF cable of 1 m length

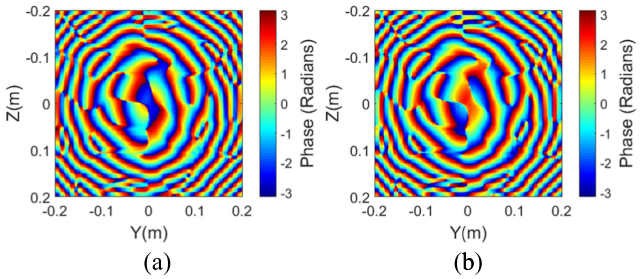

FIGURE 3. Radiated electric field phase patterns (a) with calibration and (b) without calibration.

is used to connect the antenna to the VNA. In Fig. 3, we show the phase patterns of the radiated electric fields by this antenna at 22 GHz with and without calibrating the RF cable between the antenna and the VNA. For this analysis, we import the experimental near-field scan of the antenna into the Virtualizer and use Green's functions for field propagation.

The electric field phase pattern shown in Fig. 3(a) has been calibrated to compensate for the effect of the RF cable between the VNA and the antenna, while no calibration has been applied to the field pattern shown in Fig. 3(b). As can be seen in Fig. 3, the calibrated and non-calibrated electric field phase patterns radiated by the investigated antenna have substantially different phase and hence will corrupt image reconstruction. Applying a correction to the measured signal $\mathbf{g}$ can thus compensate for the phase advance introduced by the RF path, so that the computational forward model assumed in (1) is accurate.

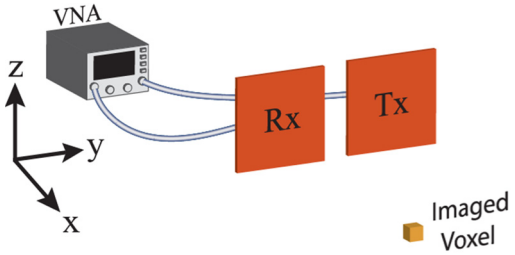

FIGURE 4. Imaging of a point source target using a small system consisting of one transmitting and one receiving frequency-diverse antennas.

In order to observe the effect of lack of calibration on image reconstruction, we first investigate a simpler configuration; a small imaging system consisting of one transmitting and one receiving antenna imaging a point source (voxel) target as depicted in Fig. 4. This analysis allows us to observe the importance of system calibration by means of analyzing the point spread function (PSF). We assume that the antennas are connected to the VNA using RF cables of 20 cm in length. Although this analysis can be done for any cable length, we choose 20 cm to be able to capture the shift in the location of the reconstructed object using a reasonably sized reconstruction volume. For imaging, the point source is placed at $x = 50$ cm distance, which remains in the radiating near-field

region of the small system depicted in Fig. 4. We perform imaging in the Virtualizer using the experimentally measured near-field scans of the antennas and use matched filter reconstruction algorithm to solve (1) and reconstruct an estimate of the scene, $\mathbf{f}_{est} = \mathbf{H}^{\dagger}\mathbf{g}$, where $\mathbf{H}^{\dagger}$ is the conjugate transpose of the $\mathbf{H}$ matrix [13]. We perform imaging with and without calibrating the system. Reconstructed images of the point source in range (x-axis) and cross-range (yz-plane) are shown in Fig. 5.

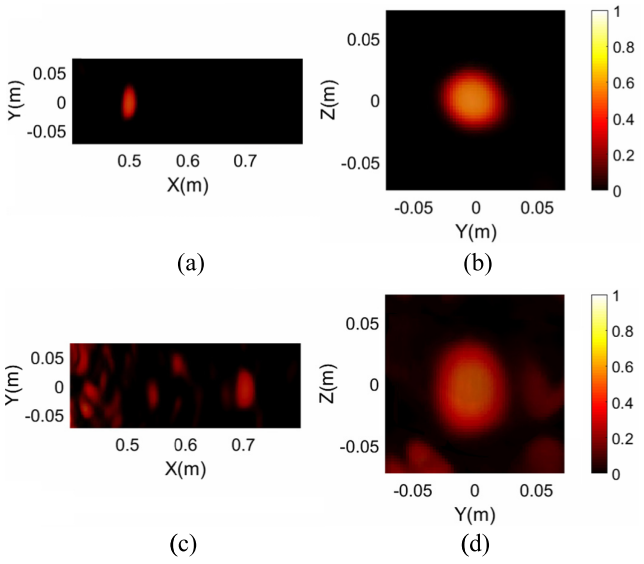

FIGURE 5. Reconstructed images. Calibrated (a) range (b) cross-range; without calibration (c) range (d) cross-range.

As can be seen in Figs. 5(a) and 5(b), the calibrated system reconstructs good quality images of the point source target in range and cross-range. However, the images that the uncalibrated system reconstructed in Figs. 5(c) and 5(d) are distorted. Analyzing Fig. 5(c), it can be seen that although both RF cables connecting the antennas and the VNA are of the same length, the result is a significant distortion in the reconstructed image, which is a direct consequence of operating in the near-field. If we were operating in the far field, we would only expect to see a shift in the reconstructed position. The cross-range reconstructed image of the point source in Fig. 5(d) is blurred and exhibits unwanted side lobes in the reconstruction. It should be mentioned here that in this analysis we used only one transmitting and one receiving antenna for the sake of simplicity. Using a larger scale system consisting of an array of transmitting and receiving antennas would increase the amount of distortion in image reconstruction when no system calibration is applied.

To compare the simulated and measured signals to achieve the system calibration, we need to ensure that the simulation model in the Virtualizer represents the experimental set-up in an accurate manner. This requires two important criteria to be satisfied: First, knowledge of the field distribution radiated by the antennas, and second, knowledge of the positions of the calibration cylinder and the antennas within the experimental system in a precise manner.

As mentioned earlier, the field distributions radiated by the antennas are found from near-field measurements over a plane, which can subsequently be propagated throughout the scene volume. To obtain the positions of the antennas and the calibration cylinder, we use a 3D optical scanning system (CREAFORM 3D Laser Scanner). The experimental imaging system together with the calibration cylinder target is shown in Fig. 6.

The small white circles on the antennas and the calibration target in Figs. 6(a) and 6(b) are optical fiducials that are used to identify the positons of the antennas and the cylinder target. By referencing these fiducials, the exact positions of the antennas and target can be precisely located and used in the Virtualizer. The optical scanner provides the positions of the optical fiducials, which can then be directly imported into the Virtualizer software. A challenging task in this process is the definition of the cylinder structure from the scanned positions of the optical fiducials, which will be explained in the next section. The full-system in Fig. 6(c) consists of eight modules, one of which is shown in Fig. 6(a) in detail. Each module has two transmitting and six receiving antennas, such that the full system consists of 16 transmitting and 48 receiving antennas. We use two ports of the VNA; the first port is connected to the transmitting distribution chain while the second port is connected to the receiving distribution chain. As depicted in Fig. 6(d), for the transmitting distribution chain we use three coaxial switches, multiplexing the first port of the VNA to accommodate the transmitting antennas. Similarly, for the receiving distribution chain, we use 11 coaxial switches accommodating the receiving antennas. Using the distribution network, we switch through all transmitting and receiving antenna pairs at 101 frequency points over the K-band, producing $M = 77,568$ measurement modes for imaging.

III. IMPLEMENTATION OF SOFTWARE CALIBRATION

In this section, we describe the specific calibration procedure used for the frequency-diverse imaging system. The first step is to define the location of the calibration cylinder within the scene. Given a cluster of points measured by the optical scanner from fiducials fixed to the surface of the cylinder target, the following procedure was used to fit the location and orientation of the cylinder in space. The location and orientation of a cylinder can be described by a three-dimensional translation and a three-dimensional rotation. The rotation is specified by an axis of rotation and a right-handed angle of rotation about this axis. This representation was chosen as it avoids the gimbal lock problem [25] when searching for the correct rotation. From the measured fiducial locations, a cylinder is constructed within the Virtualizer by first extracting the radius, orientation and location of the cylinder as follows.

The procedure is divided into two nonlinear least-squares fit steps, as performed by the Levenberg-Marquardt

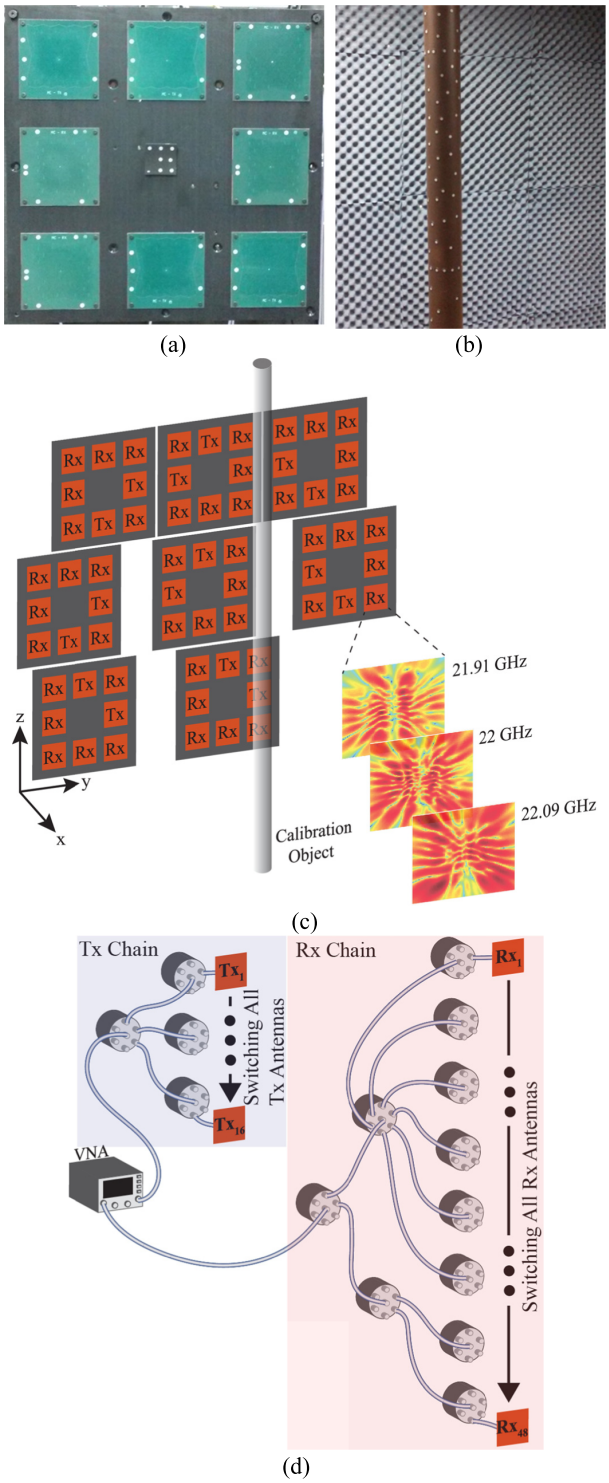

FIGURE 6. Experimental setup of the imaging system: (a) Single module consisting of 8 antennas; (b) calibration cylinder; (c) full-system consisting of 8 modules (16 transmitting and 48 receiving antennas). The radiated electric field patterns for an Rx antenna are shown for three adjacent frequencies, 21.91 GHz, 22 GHz and 22.09 GHz (d) switching chain.

algorithm [26]. The first step is to find the translation and rotation to align the cylinder with the z-axis. The primary penalty is the squared distance of each point $\mathbf{r}_i$ after translation and rotation $\mathbf{r}_i'$ from the z-axis as given by the function

$$\arg\min_{\mathbf{a},\mathbf{t},\theta} \delta\left(|\mathbf{a}|^2-1\right)^2+\sum_i \varepsilon\left|\mathbf{r}_\mathbf{i}'\cdot\hat{\mathbf{z}}\right|^2+\left|\mathbf{r}_\mathbf{i}'-\hat{\mathbf{z}}r_\mathbf{i}'\cdot\hat{\mathbf{z}}\right|^2 \tag{2}$$

where

$$\begin{aligned}\mathbf{r}_i' = {} & (\mathbf{r}_i+\mathbf{t})\cos\theta+[(\mathbf{r}_i+\mathbf{t})\times\mathbf{a}]\sin\theta \\ & +\mathbf{a}\,[(\mathbf{r}_i+\mathbf{t})\cdot\mathbf{a}]\,(1-\cos\theta)\end{aligned} \tag{3}$$

The rotation is achieved using Rodrigues' formula [27]. Additional penalties are required to resolve ambiguities, including ensuring that the length of the rotation axis vector $\mathbf{a}$ remains one (with a penalty constant δ). The cylinder may be translated along its length without changing its distance from the z-axis, a small penalty is included so that the distance from the $z=0$ plane is minimized (with a penalty constant ε). The result of the fit of the first step places the cluster of points along the z-axis, but the center of the cylinder does not necessarily correspond to the z-axis.

The second nonlinear fit step fits the axis of the cylinder and its radius. The penalty function is the difference between the squared distance between the trial axis and each point and the squared trial radius:

$$\arg\min_{\mathbf{c},R^2}\left(\left|\mathbf{r}_\mathbf{i}'-\hat{\mathbf{z}}r_\mathbf{i}'\cdot\hat{\mathbf{z}}-\mathbf{c}\right|^2-R^2\right)^2 \tag{4}$$

To aid convergence, the Jacobian of the penalty function is also specified. Once the axis of the cylinder is found, the translation $\mathbf{t}$ of the first step is adjusted to $\mathbf{t'}$ so that the cylinder axis corresponds to the z-axis after translation and rotation:

$$\mathbf{t}'=\mathbf{t}'-[\mathbf{c}\cos\theta-(\mathbf{c}\times\mathbf{a})\sin\theta+\mathbf{a}\,(\mathbf{c}\cdot\mathbf{a})\,(1-\cos\theta)] \tag{5}$$

With the rotation, translation, and cylinder radius found, a complete mesh of surface points on the cylinder visible to the antenna array may be generated. The diagram provided in Fig. 7 demonstrates a pseudocode description of the cylinder fitting procedure. The antennas were localized within the Virtualizer using a similar approach.

The defined cylinder in the Virtualizer created using the scanned fiducial points is shown in Fig. 8.

Following the definition of the calibration target and the alignment of the imaging system in the Virtualizer, the simulation configuration can be assumed to be identical to the experimental set-up except for the RF cables. Thus, we can compare the simulated, $\mathbf{g}_{s_{\text{cylinder}}}$, and measured, $\mathbf{g}_{m_{\text{cylinder}}}$, signals collected from the cylinder calibration target to calculate the additional phase advance introduced by the RF connections between the RF source and the imaging antennas. We can take the cross-correlation of these two signals in the time-domain to determine the phase. However, cross-correlation in the time-domain enforces a linear phase assumption in the RF paths. In order to avoid this assumption,

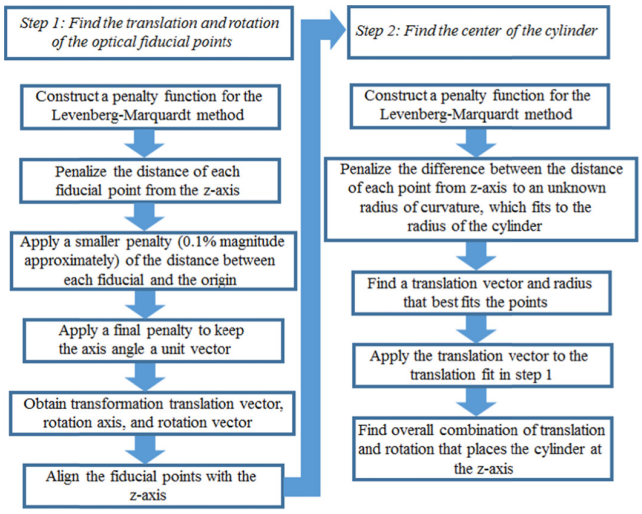

FIGURE 7. Pseudocode diagram for cylinder fitting in the Virtualizer.

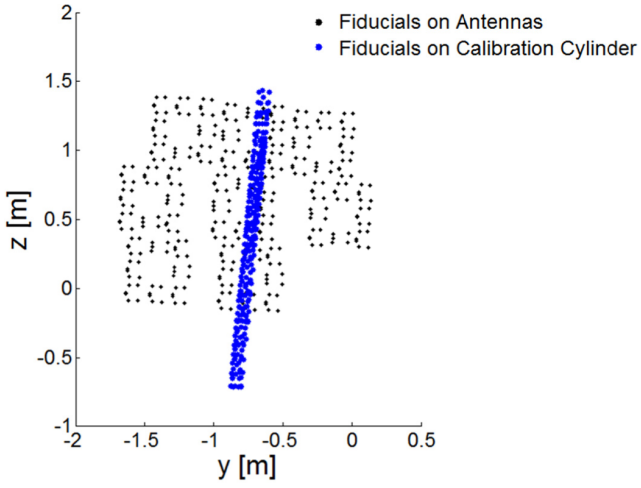

FIGURE 8. Constructed cylinder in the Virtualizer using the positions of the detected optical fiducials.

alternatively, in the frequency-domain, the phase difference between the simulated and measured signals can be calculated as follows,

$$C = \frac{\mathbf{g}_{m_{\text{cylinder}}} \mathbf{g}^*_{s_{\text{cylinder}}}}{\left|\mathbf{g}_{m_{\text{cylinder}}} \mathbf{g}^*_{s_{\text{cylinder}}}\right|} = e^{j(\phi_1 - \phi_2)} \tag{6}$$

where,

$$\mathbf{g}_{m_{cylinder}} = Ae^{j\phi_1} \tag{7}$$

$$\mathbf{g}_{s_{cylinder}} = Be^{j\phi_2} \tag{8}$$

In (7) and (8), coefficients A and B represent the amplitude of the signals (measured and simulated, respectively) received from the calibration target. Following the calculation of the calibration term, C, the experimental system can be used to image objects rather than manually determining the transmitting and receiving antenna paths individually. The calibration term, C, can be applied to the measured signal collected from an imaged object, $\mathbf{g}_m$, thus removing the phase advance, or

$$\mathbf{g}_c = \mathbf{g}_m / C \tag{9}$$

IV. IMAGING RESULTS AND DISCUSSIONS

To assess the accuracy of the proposed technique, we need to analyze the difference between the phases of the measured signals calibrated using the manual and the software calibration methods. For this comparison, we assume that the manual calibration provides the best measure of the phase advance, or the *ground truth*. However, as mentioned earlier, due to the large number of transmitting and receiving antennas, manual calibration of the full-system in Fig. 6(c) is not feasible. Therefore, for this study, we used a small system consisting of a single module as shown in Fig. 6(a), which has four transmitting and four receiving antennas, providing only 16 RF paths to be calibrated.

To achieve manual calibration of the small system in Fig. 6(a), we connect the RF cables for each transmitting and receiving path, and measure the phase response of each path, $\angle S_{21}$, using a through connection as depicted in Fig. 9.

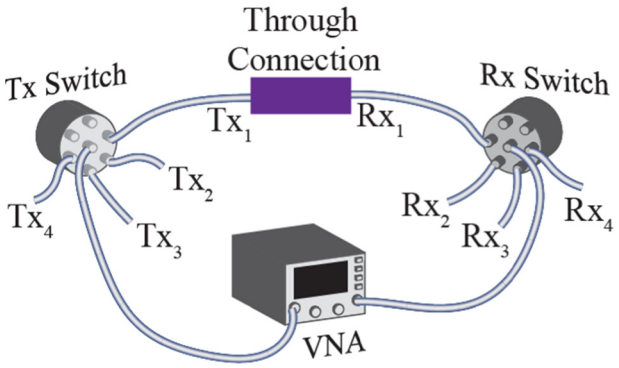

FIGURE 9. Manual calibration of the transmitting and receiving paths for the small system set-up. For depiction, connection of the first transmitting and receiving paths are shown.

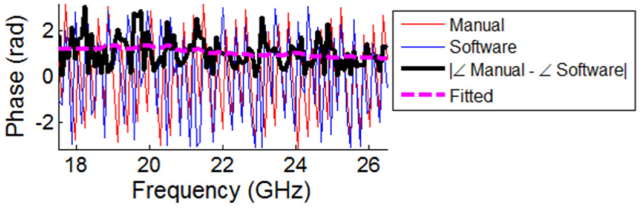

FIGURE 10. Comparison of the phase responses of the received signals calibrated using the manual and software calibration techniques for path Tx_1-Rx_3.

Ultimately, for the RF connections considered here, we expect a linear group delay across the bandwidth of operation. In Fig. 10, we compare the phase responses and the *magnitude* of the difference between the phase responses for a single transmitting and receiving path (Tx_1-Rx_3), calibrated using the manual and the proposed software calibration approaches. It should be noted that although this analysis was done for all

the 16 RF paths, to improve the readability of Fig. 10, we show only one of these paths, which was selected at random.

In Fig. 10, the manual (solid red curve) and software (solid blue curve) calibrated phase responses exhibit linearly decreasing phase, however it is difficult to observe the linear response because it is wrapped between $[-\pi, \pi]$ radians due to the long path length and the selected frequency sampling rate. Their difference, however, is a constant—within experimental variability—as clearly seen in the averaged fitted line (dashed magenta line) obtained using a digital (Savitzky-Golay) filter [28]. This suggest that we have determined an accurate calibration as a constant offset will not change the solution to (1), and therefore will have no influence on imaging. Note in Fig. 10, we consider the magnitude of the phase difference between the manual and software calibrated signals solely for clarity to remove phase wrapping associated with the values appearing near π (solid black curve).

To validate the accuracy of the proposed software calibration approach, we image an object consisting of 0.7 cm, 1 cm and 1.5 cm resolution targets using the full-system shown in Fig. 6(c). The object was attached to a polycarbonate foam stand using a small sticky tape placed on its back. The dimensions of the metal stripes forming the resolution targets were selected in accordance with the cross-range resolution of the imaging system, $\delta_{cr} \approx 0.7$ cm, calculated using the standard synthetic aperture resolution equations [4]. Discretization of the scene was done at the resolution limit, resulting in $N \approx 10,000$ voxels. In order to estimate the image using the computational imaging framework expressed in (1), we use the matched-filter technique. For this study, we first image the object with and without calibrating the system. The reconstructed images of the object are shown in Fig. 11.

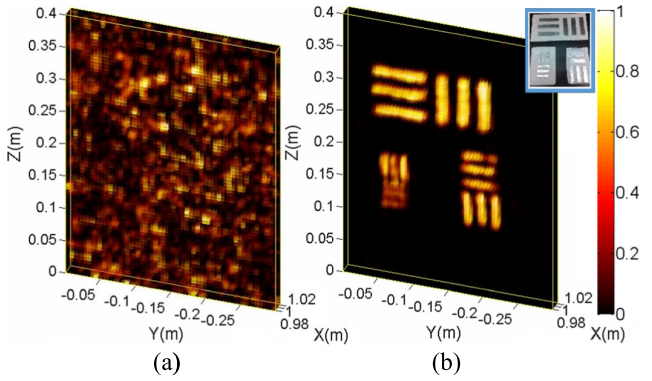

FIGURE 11. Reconstructed image of the resolution targets (a) without calibration (b) with calibration.

As can be seen in Fig 11(a), the reconstructed image obtained without calibrating the system does not contain any obviously useful information. This result underscores the importance of calibrating the RF paths to achieve near-field imaging. It can be seen in Fig. 11(b) that after calibrating the system using the proposed calibration approach, the reconstructed image of the imaged object reveals a clear outline of the resolution targets.

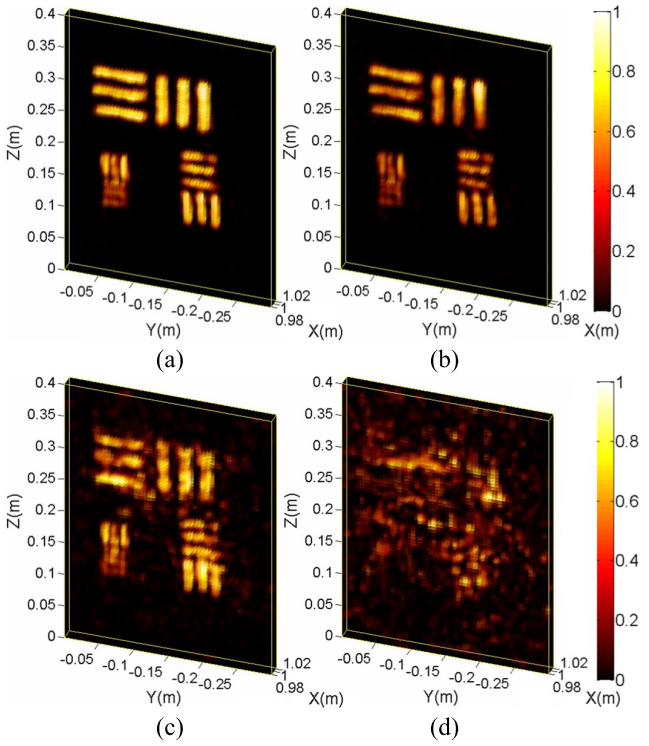

FIGURE 12. Reconstructed image of the resolution targets as a function of phase distortion applied to the calibration data (a) ±15° phase distortion (b) ±30° phase distortion (c) ±60° phase distortion (d) ±120° phase distortion.

Following the observation of the reconstructed images obtained with and without calibrating the system, we investigate the robustness of the proposed calibration technique to varying phase errors. In view of this, after calibrating the RF paths of the system using the software calibration approach, we introduce a phase distortion to the calibration data and perform imaging using the distorted calibration. The phase distortion added to the calibration data is Gaussian distributed and changes as a function of frequency. In Fig. 12, the reconstructed images of the resolution targets are shown as a function of the amount of the phase distortion introduced to the calibration data, ±15°, ±30°, ±60°, and ±120°, respectively.

As can be seen in Fig. 12(a), the image of the object reconstructed using the ±15° phase distorted calibration data is almost identical to the image reconstructed using the original (non-distorted) calibration data shown in Fig. 11(b). As shown in Fig. 12(b), although a phase distortion of ±30° degrades the reconstructed image slightly, the outlines of the resolution targets are still evident in the reconstruction. However, increasing the phase distortion above ±60° significantly affects the imaging as shown in Figs. 12(c) and 12(d). In addition to being qualitatively analyzed, it is also important that the images in Fig. 12 are quantitatively analyzed. In view of this, we can consider the reconstructed image in Fig. 11(b) as a ground truth and calculate the mean square error (MSE) for the images shown in Fig. 12 as a function of the phase

error introduced to the calibration data. Comparing the phase distorted images in Fig. 12 to the ground truth, the MSE was calculated to be 5.2% for $\pm 15^\circ$ phase distortion, 18.3% for $\pm 30^\circ$ phase distortion, 41.2% for $\pm 60^\circ$ phase distortion, and 82.9% for $\pm 120^\circ$ phase distortion. It should be noted that for the reconstructed images in Figs. 11 and 12, we plot the normalized amplitude of the reconstructed scene susceptibility vector, $\mathbf{f}$, in (1) within the range of 0-1 on a linear scale. Plotting the reconstructed images on a logarithmic scale results in 20 dB image dynamic range.

V. CONCLUSION

We have demonstrated a software approach to achieve calibration of RF paths in a frequency-diverse multistatic imaging system operating in the radiating near-field region. The proposed technique makes use of a comparison between the simulated and measured return signals from a calibration target to calculate the phase advances introduced by the RF cables. This software calibration circumvents the requirement to perform individual calibration of each transmitting and receiving path within the system manually, significantly simplifying the overall system calibration. To verify the accuracy of the proposed calibration method, we constructed two experimental systems; a small system for ground truth comparison and a full-system for imaging of a number of resolution targets. It has been demonstrated that the phase response of the system calibrated using the proposed software calibration approach is in good agreement with the ground truth. When calibrated, reconstructed images of the resolution targets reveal a clear outline of the targets. It has also been demonstrated that the proposed calibration technique is robust to phase errors of up to $\pm 30^\circ$ with a calculated image reconstruction MSE of less than 20%. The software calibration is a generic calibration scheme that can be used to calibrate any RF paths consisting of linear and non-linear components. For the presented frequency-diverse system, the antennas exhibit complex radiation patterns with nulls in the patterns, which could reduce the accuracy of the calibration. For this particular system, we could exploit the known linear response of the RF paths and apply a linearization estimation scheme on the phase data. This logical next step will be considered in the future. We also note that further improvement to the presented calibration approach could be obtained by considering the second order effects.

ACKNOWLEDGMENT

The published material represents the position of the author(s) and not necessarily that of the DHS.

REFERENCES

[1] S. Bertl and J. Detlefsen, "Effects of a reflecting background on the results of active MMW SAR imaging of concealed objects," *IEEE Trans. Geosci. Remote Sens.*, vol. 49, no. 10, pp. 3745–3752, Oct. 2011.
[2] D. M. Sheen, D. L. McMakin, and T. E. Hall, "Three-dimensional millimeter-wave imaging for concealed weapon detection," *IEEE Trans. Microw. Theory Techn.*, vol. 49, no. 9, pp. 1581–1592, Sep. 2001.
[3] O. Yurduseven, "Indirect microwave holographic imaging of concealed ordnance for airport security imaging systems," *Prog. Electromagn. Res.*, vol. 146, pp. 7–13, Apr. 2014, doi: 10.2528/PIER14032304.
[4] A. Moreira, P. Prats-Iraola, M. Younis, G. Krieger, I. Hajnsek, and K. P. Papathanassiou, "A tutorial on synthetic aperture radar," *IEEE Geosci. Remote Sens. Mag.*, vol. 1, no. 1, pp. 6–43, Mar. 2013.
[5] N. K. Nikolova, "Microwave imaging for breast cancer," *IEEE Microw. Mag.*, vol. 12, no. 7, pp. 78–94, Dec. 2011.
[6] M. Elsdon, O. Yurduseven, and D. Smith, "Early stage breast cancer detection using indirect microwave holography," *Prog. Electromagn. Res.*, vol. 143, pp. 405–419, Nov. 2013.
[7] D. Shin, A. Kirmani, V. K. Goyal, and J. H. Shapiro, "Photon-efficient computational 3-D and reflectivity imaging with single-photon detectors," *IEEE Trans. Comput. Imag.*, vol. 1, no. 2, pp. 112–125, Jun. 2015.
[8] M. F. Duarte *et al.*, "Single-pixel imaging via compressive sampling," *IEEE Signal Process. Mag.*, vol. 25, no. 2, pp. 83–91, Mar. 2008.
[9] S. S. Welsh, M. P. Edgar, R. Bowman, P. Jonathan, B. Sun, and M. J. Padgett, "Fast full-color computational imaging with single-pixel detectors," *Opt. Exp.*, vol. 21, no. 20, pp. 23068–23074, 2013.
[10] J. Hunt *et al.*, "Metamaterial apertures for computational imaging," *Science*, vol. 339, no. 6117, pp. 310–313, 2012.
[11] G. Lipworth *et al.*, "Metamaterial apertures for coherent computational imaging on the physical layer," *J. Opt. Soc. Amer. A*, vol. 30, no. 8, pp. 1603–1612, 2013.
[12] J. Hunt *et al.*, "Metamaterial microwave holographic imaging system," *J. Opt. Soc. Amer. A*, vol. 31, no. 10, pp. 2109–2119, 2014.
[13] O. Yurduseven *et al.*, "Resolution of the frequency diverse metamaterial aperture imager," *Prog. Electromagn. Res.*, vol. 150, pp. 97–107, Jan. 2015.
[14] G. Lipworth *et al.*, "Comprehensive simulation platform for a metamaterial imaging system," *Appl. Opt.*, vol. 54, no. 31, pp. 9343–9353, 2015.
[15] O. Yurduseven, V. R. Gowda, J. N. Gollub, and D. R. Smith, "Printed aperiodic cavity for computational and microwave imaging," *IEEE Microw. Wireless Compon. Lett.*, vol. 26, no. 5, pp. 367–369, May 2016.
[16] T. Fromenteze *et al.*, "Computational imaging using a mode-mixing cavity at microwave frequencies," *Appl. Phys. Lett.*, vol. 106, no. 19, p. 194104, 2015.
[17] O. Yurduseven, V. R. Gowda, J. N. Gollub, and D. R. Smith, "Multistatic microwave imaging with arrays of planar cavities," *IET Microwaves, Antennas Propag.*, doi: 10.1049/iet-map.2015.0836.
[18] O. Yurduseven, J. N. Gollub, D. L. Marks, and D. R. Smith, "Frequency-diverse microwave imaging using planar mills-cross cavity apertures," *Opt. Exp.*, vol. 24, no. 8, pp. 8907–8925, 2016.
[19] D. L. Marks, J. Gollub, and D. R. Smith, "Spatially resolving antenna arrays using frequency diversity," *J. Opt. Soc. Amer. A*, vol. 33, no. 5, pp. 899–912, 2016.
[20] M. Ostadrahimi *et al.*, "Analysis of incident field modeling and incident/scattered field calibration techniques in microwave tomography," *IEEE Antennas Wireless Propag. Lett.*, vol. 10, pp. 900–903, Sep. 2011.
[21] C. Gilmore, A. Zakaria, P. Mojabi, M. Ostadrahimi, S. Pistorius, and J. L. Vetri, "The University of Manitoba microwave imaging repository: A two-dimensional microwave scattering database for testing inversion and calibration algorithms [measurements corner]," *IEEE Antennas Propag. Mag.*, vol. 53, no. 5, pp. 126–133, Oct. 2011.
[22] S. S. Ahmed, *Electronic Microwave Imaging With Planar Multistatic Arrays*. Berlin, Germany: Logos Verlag Berlin GmbH, 2014.
[23] M. Pastorino, *Microwave Imaging*, 1st ed. New York, NY, USA: Wiley, 2010.
[24] J. Andrews and C. H. Séquin, "Type-constrained direct fitting of quadric surfaces," *Comput.-Aided Design Appl.*, vol. 11, no. 1, pp. 107–119, Sep. 2013.
[25] F. L. Markley and M. D. Shuster, "A new angle on the euler angles," in *Proc. Flight Mech. Estimation Theory Symp.*, Greenbelt, MD, USA, May 1995, pp. 395–403.
[26] H. P. Gavin, "The Levenberg–Marquardt method for nonlinear least squares curve-fitting problems," Dept. Civil Environ. Eng., Duke Univ., Durham, NC, USA, Tech. Rep., Oct. 2013.
[27] R. M. Murray, Z. Li, S. S. Sastry, and S. S. Sastry, *A Mathematical Introduction to Robotic Manipulation*. Boca Raton, FL, USA: CRC Press, 1994.
[28] J. S. Orfanidis, *Introduction to Signal Processing*. Englewood Cliffs, NJ, USA: Prentice-Hall, 1996.

OKAN YURDUSEVEN (S'09–M'11) received the B.Sc. and M.Sc. degrees in electronics and communications engineering from Yildiz Technical University, Istanbul, Turkey, in 2009 and 2011, respectively, and the Ph.D. degree in electromagnetics from Northumbria University, Newcastle upon Tyne, U.K., in 2014.

He was a part-time Lecturer with the Faculty of Engineering and Environment, Northumbria University, from 2011 to 2014. Since 2014, he has been a Post-Doctoral Associate with the Center for Metamaterials and Integrated Plasmonics, Department of Electrical and Computer Engineering, Duke University. His research interests include antennas and propagation, antenna measurement techniques, microwave and millimeter-wave imaging, frequency-diverse imaging, metamaterials, and wireless power transfer. He has authored or co-authored over 50 papers in peer-reviewed international journals and conference proceedings.

Dr. Yurduseven received a best paper award at the Mediterranean Microwave Symposium in 2012. He also received an Academic Excellence Award from the Association of British—Turkish Academics in London in 2013. He is a member of the European Association on Antennas and Propagation. He serves as a Reviewer of the IEEE TRANSACTIONS ON ANTENNAS AND PROPAGATION, the IEEE TRANSACTIONS ON MICROWAVE THEORY AND TECHNIQUES, and the IEEE ANTENNAS AND WIRELESS PROPAGATION LETTERS.

JONAH N. GOLLUB (M'16) received the B.A. degree in physics from Reed College, in 2000, and the Ph.D. degree in physics from the University of California, San Diego, in 2009. His thesis work involved in characterizing the hybridization of metamaterials with magnetic materials. From 2010 to 2012, he was a Lead Modeling and Simulation Scientist at a startup company developing surface metamaterials with applications targeted toward imaging and biological detection under DARPA, MDA, the Army, and NSF funded efforts. He joined Duke University as a Research Scientist in 2013, where he is currently focused on developing real-time millimeter wave imaging approaches which utilize frequency diverse antennas and compressive imaging techniques.

KENNETH P. TROFATTER received the B.Eng. degree in engineering physics and the B.Eng. degree in computer science from the University of Tennessee Knoxville, in 2011. He joined the Dr. D. Smith's Research Group, Duke University, in 2013, as a Lab Technician, supporting the research and development of novel microwave compressive sensing imaging funded by the DHS. Recently, he has transitioned into graduate study with Duke University as an Electrical and Computer Engineering Ph.D.

DANIEL L. MARKS was born in Chicago, IL, in 1973. He received the B.S., M.S., and Ph.D. degree from the University of Illinois at Urbana–Champaign, in 1995, 1998, and 2001, respectively. From 2001 to 2008, he was a Research Scientist with the Biophotonics Laboratory, University of Illinois at Urbana–Champaign. He is currently an Associate Research Professor with the Department of Electrical and Computer Engineering, Duke University, where he joined in 2009. He has authored 85 research articles, 17 patents, and has been an Editor of *Applied Optics*. His research interests include optics, optical design, computational imaging, millimeter-wave and terahertz imaging, metamaterials, and synthetic electromagnetic structures.

ALEC ROSE received the B.S. degree in physics from Boston College, in 2009, and the Ph.D. degree in electrical and computer engineering from Duke University, in 2013, under the guidance of Prof. D. R. Smith.

As a member of the Smith Research Group, he made contributions to the fields of nonlinear electromagnetic metamaterials and plasmonics. He has since become the Director of Advanced Development with Evolv Technologies, Inc., a startup company in Waltham, MA, working to advance millimeter-wave sensing systems for physical security applications.

Dr. Rose received the Outstanding ECE Ph.D. Dissertation Award from Duke University in 2013 for this thesis, Theory and Design of Nonlinear Metamaterials.

DAVID R. SMITH (M'03) is currently the Department Chair and James B. Duke Professor of Electrical and Computer Engineering with Duke University and the Director of the Center for Metamaterials and Integrated Plasmonics. He is an Adjunct Professor with the Physics Department, University of California at San Diego, an Affiliate Faculty Member with the Electrical and Computer Engineering Department, University of Washington, and a Visiting Professor of Physics with Imperial College, London.

He received the Ph.D. degree in physics from the University of California at San Diego (UCSD), in 1994. His research interests include the theory, simulation, and characterization of unique electromagnetic structures, including photonic crystals and metamaterials, as well as applications of such materials.

While at UCSD, he and his colleagues demonstrated the first left-handed (or negative index) metamaterial at microwave frequencies in 2000. He has more than 200 publications on matematerials and plasmonics, and was selected by ISI-Reuters as a Citation Laureate in 2009 for the most number of highly cited papers in the field of physics over the last decade. He was once again recognized as one of the Highly Cited Researches 2014 by ISI-Reuters in the category of physics.

In 2002, he was elected as a member of The Electromagnetics Academy. In 2005, he was part of a five member team that received the Descartes Research Prize by the European Union for their contributions to metamaterials and other novel electromagnetic materials. He also received the Stansell Research Award from the Pratt School of Engineering at Duke University in 2005. In 2006, he was selected as one of the Scientific American 50, a group recognized by the editors of Scientific American for achievements in science, technology, and policy. His work has twice appeared on the cover of Physics Today, and twice has been selected as one of the Top Ten Breakthroughs of the year by *Science Magazine*. In 2013, he was a co-recipient of the James C. McGroddy Prize for New Materials by the American Physical Society.

In 2006, he, along with colleague Sir John Pendry, suggested metamaterials could be used to design an electromagnetic cloak, introducing the new design tool of transformation optics. In 2013, he was asked to write an op-ed piece for the New York Times on cloaking research.

In 2013, he served as a Founding and Acting Director of the Metamaterials Commercialization Center, a unit within the Intellectual Ventures (Bellevue, WA) dedicated to commercializing metamaterials concepts. He serves on the Advisory Board for Kymeta, which targets metamaterial-based antennas for satellite communications, and is a Co-Founder of Evolv Technologies Inc., which targets metamaterial apertures for security screening applications, as well as Echodyne, which is seeking to apply metamaterial apertures to radar applications.